

Correlations in parameter estimation of low-mass eccentric binaries: GW151226 & GW170608

Eamonn O’Shea^{1,*} and Prayush Kumar^{1,2}

¹*Cornell Center for Astrophysics and Planetary Science,
Cornell University, Ithaca, New York 14853, USA*

²*International Centre for Theoretical Sciences, Tata Institute of Fundamental Research, Bangalore 560089, India*
(Dated: July 19, 2021)

The eccentricity of binary black hole mergers is predicted to be an indicator of the history of their formation. In particular, eccentricity is a strong signature of dynamical formation rather than formation by stellar evolution in isolated stellar systems. It has been shown that searches for eccentric signals with quasi-circular templates can lead to loss of SNR, and some signals could be missed by such a pipeline. We investigate the efficacy of the existing quasi-circular parameter estimation pipelines to determine the source parameters of such eccentric systems. We create a set of simulated signals with eccentricity up to 0.3 and find that as the eccentricity increases, the recovered mass parameters are consistent with those of a binary with up to a $\approx 10\%$ higher chirp mass and mass ratio closer to unity. We also employ a full inspiral-merger-ringdown waveform model to perform parameter estimation on two gravitational wave events, GW151226 and GW170608, to investigate this bias on real data. We find that the correlation between the masses and eccentricity persists in real data, but that there is also a correlation between the measured eccentricity and effective spin. In particular, using a non-spinning prior results in a spurious eccentricity measurement for GW151226. Performing parameter estimation with an aligned spin, eccentric model, we constrain the eccentricities of GW151226 and GW170608 to be < 0.15 and < 0.12 respectively.

I. INTRODUCTION

As of 2021, the Laser Interferometer Gravitational-wave Observatory (LIGO) and the Virgo observatory have detected gravitational wave (GW) signals from dozens of binary black hole (BBH) mergers during their first three observing runs [1]. As the field of gravitational wave astronomy moves forward, the network of Earth-based detectors will be joined by KAGRA [2] and LIGO India [3] in the coming few years, and possibly followed up by third-generation instruments such as the Cosmic Explorer (CE) [4] and the Einstein Telescope (ET) [5]. Expanding the network to include more geographical locations will improve the sky localization of events, and the increased sensitivity of future detectors (CE and ET) will increase our detection rates, particularly at lower frequencies.

The mechanisms of formation and merging of these binary systems are the subject of active research [6–9]. One possibility is that of isolated binary formation, either through formation of a common envelope phase [10–12], or through chemically homogeneous evolution [13, 14]. This formation channel generally results in black holes with lower masses, $\lesssim 50 M_{\odot}$, and aligned spins [15].

Another possible formation channel that can account for the rate of mergers seen is that of dynamical binary evolution in dense globular clusters [16–20] or in AGN disks [21–23]. In the case of dense environments, binary black holes merge after undergoing many interactions with third bodies or other binaries. Dynamical

interactions can produce multiple generations of mergers. Such formation channels lead to binaries with higher mass [24, 25] that can lie in the supernova pair-instability mass gap [26, 27], isotropic spins [18, 28], and eccentricity [29–31]. In such cases the eccentricity of a binary can be driven to non-zero values through the Lidov-Kozai effect [32, 33]. By performing Monte Carlo simulations of such dense clusters, it has been shown [34, 35] that on the order of 5% of mergers in globular clusters can have eccentricity > 0.1 when the frequency of their orbits enters the sensitivity band of terrestrial GW detectors at 10 Hz. Interactions within AGN disks can also lead to binaries with measurable eccentricity [36, 37]. Orbital eccentricity is therefore striking evidence that can conclusively establish dense clusters as breeding grounds for compact binary mergers.

The presence of eccentricity in any of the gravitational waveforms seen thus far has yet to be conclusively established. Direct searches for eccentric neutron-star candidates in LIGO’s O2 data have yielded no detections [38–40]. There have also been studies [41, 42] to measure orbital eccentricities of merger events in GWTC-1, and the eccentricities of the two neutron star events [43]. While they agree that most observed GW signals are sourced from quasi-circular binary mergers, one of the studies finds evidence of residual orbital eccentricity in a couple of events [42]. There is statistical evidence that at least one merger in GWTC-2 is the result of hierarchical mergers [9] and that GW190521 is favoured to have formed from the merger of second generation black holes [44], or possibly through dynamical capture [45]. There is some evidence that it could be the result of an eccentric merger [46], although it could be indistinguishable from a precessing, quasi-circular binary merger [47] given the

* edo27@cornell.edu

short length of the signal.

Our ability to accurately determine the eccentricity of mergers such as GW190521 [39] should increase as the network of detectors expands to include deciHertz detectors [48, 49]. It has been shown that the addition of detectors such as Cosmic Explorer and the Einstein Telescope will increase signal-to-noise ratio (SNR) of eccentric signals, in some cases to higher SNRs than similar quasi-circular systems [50].

There has been previous work to investigate the effect that eccentric signals can have on the detectability of eccentric signals when the quasi-circular template banks that LIGO/Virgo currently employs are used [51, 52]. Mildly eccentric systems can still be detected by the pipelines, but with a loss of SNR. However, moderately eccentric ($e_0 > 0.275$) systems would likely be missed by search pipelines [53]. Once detected, ignoring eccentricity could still lead us to infer with biases other intrinsic parameters of the source.

In this paper we pursue two related goals. The first is to understand how our lack of inclusion of orbital eccentricity in waveform templates alters our inference on the source parameters of GW signals. To this end we simulate a set of eccentric inspiral-merger-ringdown (IMR) signals and perform Bayesian parameter estimation on them using waveform templates that represent binary mergers on quasi-circular orbits. We find that as we increase the orbital eccentricity of GW sources, our quasi-circular templates furnish larger chirp mass values and less asymmetric mass ratios than the those simulated. Although eccentricity alters the rate of inspiral in the same way a larger chirp mass does [54], it also introduces modulations in the orbital frequency as a function of time to make the phase evolution qualitatively very different from what a shift in binary masses does. This bias is therefore not obvious, especially when considering the full inspiral-merger-ringdown. We quantify the bias to find an $\mathcal{O}(10\%)$ drift in chirp mass measurement alone in the case of low-mass binaries with moderate SNRs (20-30), which is significant given that the measurement precision on the chirp mass is smaller than $\mathcal{O}(1\%)$. We also find a similarly significant bias in the measurement of binary mass ratio. Our quantitative findings are consistent with previous results [43, 55].

Our second goal is to investigate whether this bias appears with real GW events [56]. To this end, we show that GW151226 and GW170608 are possibly eccentric binary mergers, as Ref. [42] found and Ref. [41] disputed. In particular, we find that if we use a non-spinning, eccentric waveform approximant to perform parameter estimation, GW151226 is consistent with a moderately eccentric event, with a chirp mass that is an underestimate of that found by the LVC [57]. However, if we use an eccentric model that also allows for black hole spins (aligned with the orbital angular momentum, i.e. non-precessing), GW151226 is consistent with a non-eccentric event with non-zero spin, in agreement with the LVC [57]. The implication that the eccentricity measurement can be cor-

related with the measured masses *and* spins implies that non-spinning eccentric approximants may be insufficient for the measurement of eccentricities of binary black holes, especially if the objects are spinning.

In Section II we describe our methods, including a description of the waveform models we use in II A. In Section II B we describe the setup for our parameter estimation runs using BILBY. Section III C details the eccentric simulated signals and results of their recovery with quasi-circular templates. In section III B we employ a full IMR, eccentric waveform to perform parameter estimation on the two GW events described above, with and without spins included in our prior. We follow up our studies on real events in Section III C by simulating the best fit quasi-circular parameters for these events, and performing inference with the same eccentric IMR model to determine how their parameters would be recovered if they were truly non-eccentric.

Throughout, we refer to mass as measured in the detector frame. We denote eccentricity as e_0 , meaning eccentricity at a particular reference frequency.

II. METHODS

A. Waveform models

Detection and characterization of the source properties of eccentric signals require accurate and efficient waveform models. Some of the existing waveform models use a post-Newtonian description and only predict the inspiral portion of the signal, such as the `EccentricFD` [58] and `EccentricTD` [59], which are both implemented in LALsuite [60]. Recently, models have been developed to produce full inspiral-merger-ringdown (IMR) waveform for eccentric binaries, by hybridizing eccentric inspiral signals with a quasi-circular merger-ringdown portion (`ENIGMA`) [53], through an effective one-body (EOB) formalism [61, 62], or by surrogate modelling of numerical relativity waveforms [63].

The first eccentric model we use is the inspiral portion of `ENIGMA` [53]. `ENIGMA` is a time-domain model designed to produce full inspiral-merger-ringdown waveforms up to moderate eccentricities. `ENIGMA` incorporates corrections for the energy flux of quasi-circular binaries and gravitational self-force corrections to the binding energy of compact binaries up to 6PN order. Higher-order corrections to the effect of the inclination angle on the inspiral waveform were introduced in [50]. The framework coincides with the TaylorT4 approximant at 3PN order in the zero-eccentricity limit. We opt to use the inspiral portion of the model alone in our analyses, for reasons elaborated in Appendix A. In order to produce the inspiral waveform, we integrate the equations of motion from [53] until the expansion parameter $x = (M\omega)^{2/3}$, reaches the Schwarzschild innermost stable circular orbit (ISCO), at $x_{ISCO} = \frac{1}{6}$. Here, M is the total mass of the binary and ω is the mean orbital frequency. We refer the

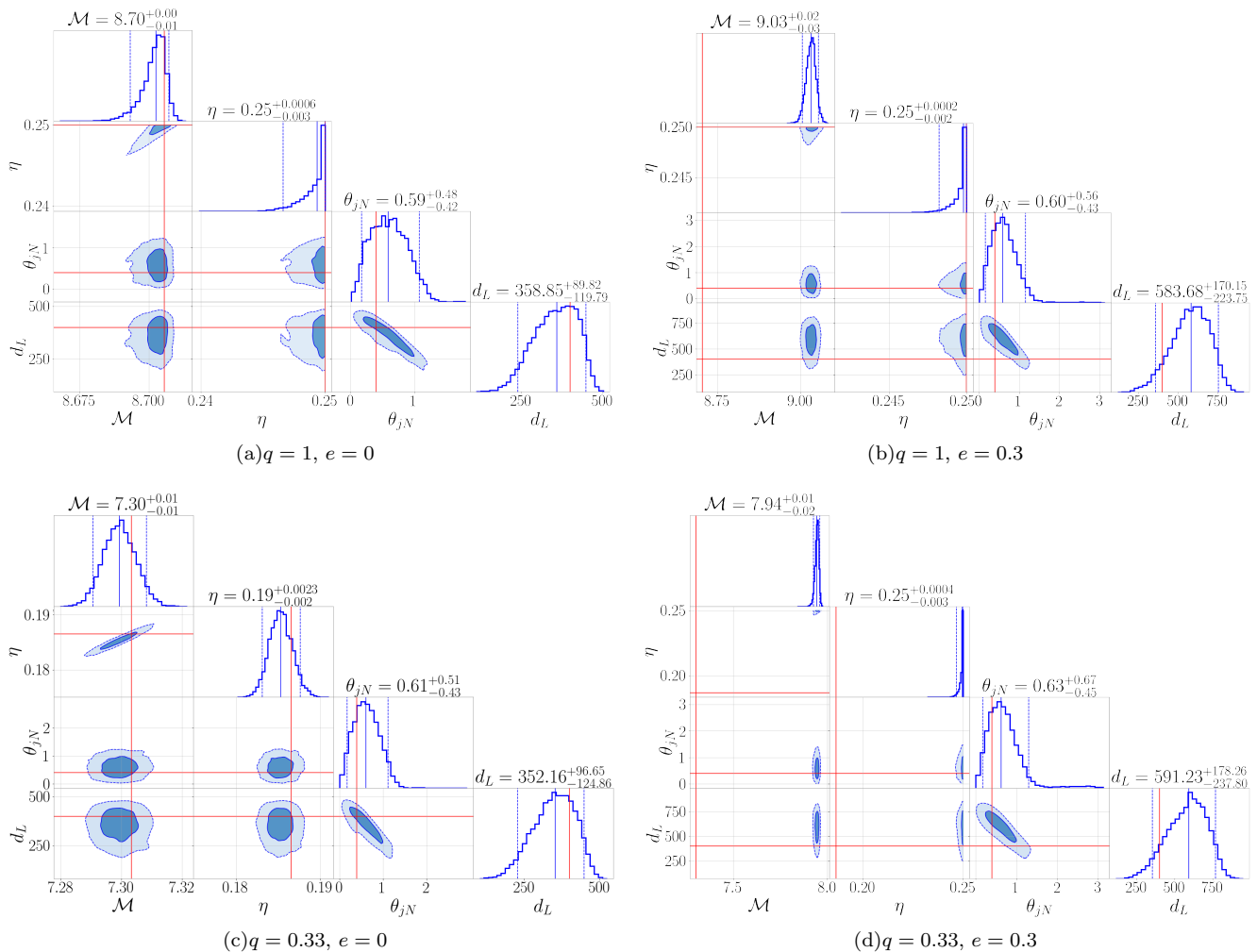


FIG. 1. Comparison of parameter estimation results for simulated signals of zero and moderate eccentricity using **IMRPhenomD** as the likelihood model and **TEOBResumE** as the signal model. Shown are the posterior distributions of chirp mass \mathcal{M}_c , symmetric mass ratio η , luminosity distance D_L and inclination ι , where the red lines indicate signal’s values.

reader to [50, 53] for more details.

The second waveform model we use is an extension of the full IMR quasi-circular model **TEOBiResumS_SM** [64] to include eccentric effects, which was introduced in [65]. This model, which we will refer to as **TEOBResumE**, alters the angular momentum flux portion of **TEOBiResumS_SM** with a Newtonian-like prefactor, which generalizes the quasi-circular model to moderate eccentricities ($e \approx 0.3$). We have used the publicly available implementation at [66]¹ without any changes to the core routines, and use the dominant waveform modes in our analyses. However, we have loosened the absolute and relative error tolerances of its ODE integrator from their default values of 10^{-13} and 10^{-11} to 10^{-8} and 10^{-7} . We find that this allows the likelihood function to be evaluated on the

$\mathcal{O}(10^{-2}$ s) timescale, which makes full parameter estimation analyses viable. To ensure that loosening this tolerance does not significantly degrade the produced waveforms, we calculate the mismatch,

$$M = 1 - \frac{\langle h_{\text{strict}} | h_{\text{loose}} \rangle}{\langle h_{\text{strict}} | h_{\text{strict}} \rangle} \quad (1)$$

between the stricter waveform h_{strict} and the looser waveform h_{loose} , where we use the straightforward inner product between two timeseries

$$\langle a | b \rangle = \int a(t)b(t)dt. \quad (2)$$

We find that waveform generation is robust to such changes with the ODE integrator, and the mismatches differ by no more than 10^{-3} over the parameter space.

Although this waveform model can produce waveforms with higher-order modes, we have opted to only use the dominant (2, 2) mode in this study.

¹ Using the `eccentric` branch with commit 10f6110

B. Parameter estimation

We use the python package `BILBY` [67] to simulate the signals and perform parameter estimation. `BILBY` calculates the posterior distribution $p(\boldsymbol{\theta}|y)$ for the set of source parameters $\boldsymbol{\theta}$ given the data y , according to Bayes' theorem, $p(\boldsymbol{\theta}|y) \propto p(y|\boldsymbol{\theta})p(\boldsymbol{\theta})$ where $p(y|\boldsymbol{\theta})$ is the likelihood and $p(\boldsymbol{\theta})$ is the prior. The likelihood function for a set of N detectors is the standard used for gravitational wave astronomy:

$$p(y|\boldsymbol{\theta}) = \exp\left(-\frac{1}{2}\sum_{i=1}^N \langle \hat{y}_i(f) - \hat{s}_i(f, \boldsymbol{\theta}) | \hat{y}_i(f) - \hat{s}_i(f, \boldsymbol{\theta}) \rangle\right), \quad (3)$$

where $\hat{y}_i(f)$ and $\hat{s}_i(f, \boldsymbol{\theta})$ are the frequency-domain representations of the data and the model waveform. The inner product $\langle \cdot | \cdot \rangle$ is given by

$$\langle \hat{a}_i(f) | \hat{b}_i(f) \rangle = 4\text{Re} \int_{f_{\min}}^{f_{\max}} \frac{\hat{a}_i(f)\hat{b}_i^*(f)}{S_n^i(f)} df, \quad (4)$$

with the weight factor $S_n^i(f)$ being the advanced LIGO power spectral density (PSD). Superscript i labels the detector, in our case either LIGO Hanford or LIGO Livingston. We use the zero-detuning high-power noise curves [68]. The interpretation of this likelihood function is that a given candidate waveform is likely to be present in the data, if subtracting it from the data resembles colored Gaussian noise.

We sample from the posterior distribution using a nested sampling algorithm implemented via the `dynesty` package [69] in `BILBY`. We use 1,000 live points, and a stopping criterion of $\Delta \log \mathcal{Z} < 0.1$ where \mathcal{Z} is the estimated Bayesian evidence. To improve efficiency, we use the option in `BILBY` to analytically marginalize over the coalescence time [70], coalescence phase [71] and distance [72] in the calculation of the likelihood in Eq. (3), and then reconstruct the posterior for these parameters after the maximum likelihood calculation has completed.

III. RESULTS

A. Simulated signals

We have already observed binary black hole mergers with masses ranging from 14 M_\odot to 160 M_\odot [73]. In this study, we focus on binaries at the lower end of this spectrum, as a longer inspiral signal will have a stronger eccentric signature. Also, at lower masses the inspiral of the signal dominates the SNR as compared to the merger portion, which allows us to draw reliable conclusions using inspiral-only waveform models.

Since our goal is to understand the biases of existing GW parameter estimation pipelines that use quasi-circular waveforms as filter templates, we limit our waveform models in the likelihood evaluation to be

Parameter	Simulated value
q	{ 1, 0.5, 0.33 }
e	{ 0, 0.001, 0.01, 0.05, 0.1, 0.2, 0.3 }
M_T	20. M_\odot
D_L	400 Mpc
ι	0.4
α	0
δ	0
ψ	0
ϕ_c	0
t_c	7 s
Network SNR	21-33

TABLE I. Simulated signals values for the mass ratio q , eccentricity e , total mass M_T , luminosity distance D_L , inclination ι , right ascension α , declination δ , polarization ψ , coalescence phase ϕ_c , and coalescence time t_c .

Parameter	Prior	Range
q	Uniform	0.25–1.
M_c	Uniform	5– 10 M_\odot
D_L	Uniform Comoving	10–1000 Mpc
ι	Uniform sin	0– π
α	Uniform	0– 2π
δ	Uniform cos	$-\pi/2$ – $\pi/2$
ψ	Uniform	0– π
ϕ_c	Uniform	0– 2π
t_c	Uniform	0–8

TABLE II. Priors used in the parameter estimation for the mass ratio q , chirp mass \mathcal{M}_c , luminosity distance D_L , inclination ι , right ascension α , declination δ , polarization ψ , coalescence phase ϕ_c , and coalescence time t_c .

`SEOBNRv4_ROM` [74] and `IMRPhenomD` [75, 76]. Since the waveforms produced with our modified `ENIGMA` model are inspiral-only, we also utilise the PN quasi-circular model `TaylorF2` to rule out any biases that may arise comparing to inspiral-merger-ringdown templates. Using 3 waveform models for the likelihood, 2 waveform models for the signals, and the direct product of the parameters described in Table I gives us 126 signals on which to perform parameter estimation. As a control, we also study a further set of six signals using `ENIGMA-Inspiral` as the waveform approximant for the signal *and* likelihood evaluation, with $q = 0.5$ and the eccentricity taking the values in Table I. The priors for all the parameter estimation analyses are shown in II. We use a non-spinning prior for our simulated signals since the majority of the black holes detected thus far have had negligible spins.

Each of these signals is generated from a starting frequency 15 Hz using the given waveform model, and then injected into zero noise. As described in Appendix C of [77], using zero noise eliminates the biases in parameter estimation that can be caused by a particular noise realization. The data is sampled at 2048 Hz, and we use the two-detector network of LIGO Hanford and Livingston, with their design sensitivity PSD's used to cal-

culate the likelihood evaluation given by Eq. (3). In the calculation of the likelihood, we use $f_{min} = 20$ Hz. We sample in chirp mass and mass ratio, rather than component masses. We use sampling priors shown in Table II. At a luminosity distance of 400 Mpc, the signals are relatively loud, and have a two-network SNR ranging from 21 to 33 at design sensitivity.

We start the discussion with Figure 1 where we show the posterior distributions recovered for four representative simulated binary mergers. The signal waveform model is **TEOBResumE**, which we expect to be the best example since it is a full IMR model, with zero and nonzero eccentricity, and the mass ratios $q = 1$ and $q = 0.33$. We opt to plot the symmetric mass ratio $\eta = \frac{q}{(1+q)^2}$, instead of q in this section as it is the parameter that appears to leading order in a PN expansion.

In the $e = 0$ cases, **IMRPhenomD** well recovers all of the component parameters. Since these signals are high SNR and have a long inspiral, the chirp mass is extremely precisely and accurately estimated, with the 90% confidence interval within less than 0.1% of the simulated value.

The $e = 0.3$ cases, however, show a very precise but inaccurate inference of the chirp mass, with the quasi-circular template drastically *overestimating* its value. The median recovered value deviates from the simulated value by $\approx 3\%$, whereas the 90% confidence interval is about 0.2% of the median estimated value. η is well determined to be $\frac{1}{4}$ in both the eccentric and non-eccentric cases. Moreover, in the asymmetric mass, non-eccentric case, the correct value of η is inferred within our error-estimates. However, when the simulated signal is asymmetric and eccentric, the value of η is confidently and incorrectly inferred to be that of a symmetric binary.

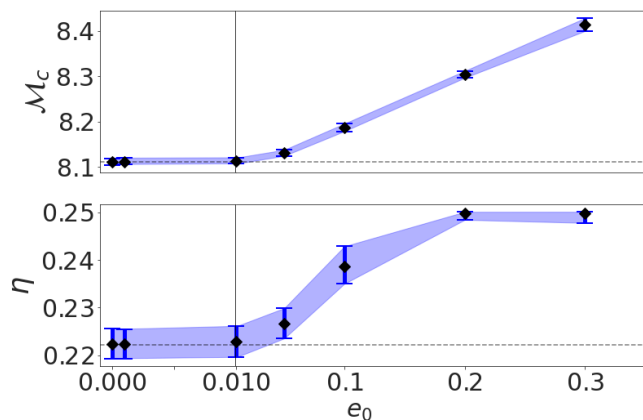


FIG. 2. Recovery of chirp mass \mathcal{M}_c and symmetric mass ratio η at different eccentricities for a $q = 0.5$ binary, when using **ENIGMA-Inspiral** as both template and signal model. Horizontal dashed lines indicate the value of the parameter for the signal. Error bars are 90% confidence intervals, with diamonds denoting the median recovered value. The shaded region connecting the errorbars is to illustrate the trend. Note the different scales between $[0., 0.01]$ and $[0.01, 0.3]$ on the x -axis.

Figure 2 illustrates these trends for the case of using **ENIGMA-Inspiral** for both the signal and parameter estimation. At low eccentricities, the mass parameters are correctly recovered, but at higher eccentricities, the recovered parameters are those of a heavier, symmetric binary.

1. Chirp Mass Recovery

Figure 3 summarizes the chirp mass estimates for the rest of our simulated signals, showing the six combinations of signal and recovery waveform models. The top row shows the case where the simulated signal is generated with the IMR model, **TEOBResumE**, and the bottom row with the inspiral model **ENIGMA-Inspiral**.

Let us consider the top row, where **TEOBResumE** is used for the signal. No matter the template model, we find a systematic bias in chirp mass recovery that increases in proportion to orbital eccentricity. When **TaylorF2** is used as the waveform model for templates, the error bars are wider due to the missing merger-ringdown portion. Also in the $e_0 = 0$ case, there is a slight bias in the **TaylorF2** recovery due the missing merger. But since we see very similar results in the case of **SEOBNRv4_ROM** and **IMRPhenomD**, we conclude that this result is invariant under a change of waveform family.

Let us now consider the bottom row, using **ENIGMA-Inspiral** for the signal. In the left and middle panels, when using IMR models for inference, we see a small bias in chirp mass recovery even at $e_0 = 0$. This comes from the merger-ringdown portion of the IMR templates fitting to the last few cycles of the **ENIGMA-Inspiral** signal, resulting in a lower chirp mass. We see no such bias in the **TaylorF2** case at $e_0 = 0$.

For each combination of signal and recovery model there is a clear trend: as the eccentricity of the simulated signal increases, the circular templates strongly overestimate the chirp mass beyond the values within the 90% credible intervals. The effect becomes more pronounced at higher eccentricities, and the maximum fractional deviation over the dataset is $\sim 9\%$.

2. Mass Ratio Recovery

Figure 4 shows the effects of increasing eccentricity on the estimation of the symmetric mass ratio, η . Overall, the trend is less systematic than in the case of the chirp mass.

Again, consider the top row with **TEOBResumE** signals. At $e_0 = 0$, the recovered η agrees well with the simulated value. One thing we notice is there is a jump in the recovered η when the eccentricity changes from $e_0 = 0$ to $e_0 = 10^{-3}$. This is due to a slight discontinuity in the **TEOBResumE** waveform as the eccentricity goes to 0. For small eccentricities, $e_0 \leq 0.01$, there is good agreement between **TEOBResumE** and **SEOBNRv4_ROM**. There is

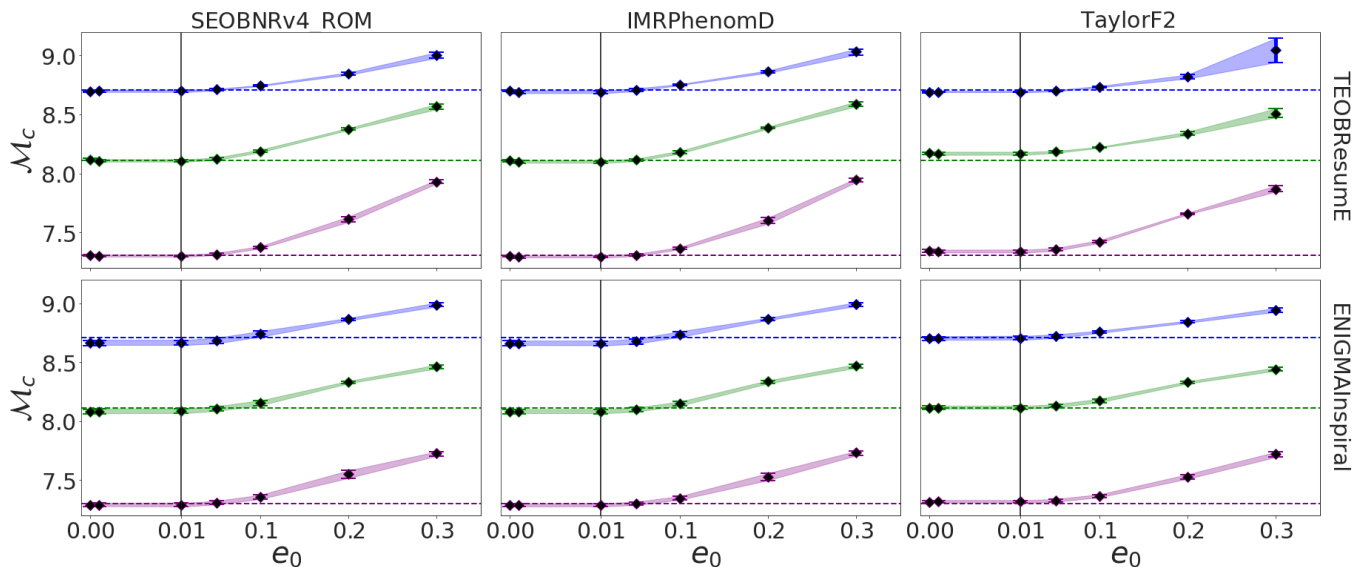


FIG. 3. Estimated values of the chirp mass for signals at different eccentricities. Dashed lines indicate the value of the simulated signal. The colors blue, green and purple correspond to the $q = 1, 0.5, 0.33$ signals respectively. The bars represent the 90% confidence intervals, with the diamond representing the median value. The shaded connects the ends of the error bars to illustrate the upward trend. The labels on top specify which model was used in the parameter estimation, and the labels on the right side of the figure specify which model was used to simulate the signal. Note the different scales between $[0., 0.01]$ and $[0.01, 0.3]$ on the x -axes.

a slight bias when $e_0 \leq 0.01$ in the IMRPhenomD case, since the Phenom family of waveforms is constructed differently from the EOB family. In the TaylorF2 case, the recovered η is overestimated as compared to the simulated value except for $\eta = \frac{1}{4}$. This systematic bias is due to the lack of the merger-ringdown portion in the templates.

Now consider the bottom row of ENIGMA-Inspiral signals. In both the SEOBNRv4_ROM and IMRPhenomD case, we see the recovered η is underestimated compared to that of the simulated signal. Again this is because the full IMR templates fit their merger-ringdown portion to the last few cycles of the inspiral-only signal. In these cases the bias in recovery between IMR templates with an inspiral signal is greater than the bias caused by using different waveform families. The bias at $e_0 = 0$ is much reduced in the case of TaylorF2, since the signal and templates are inspiral-only. However there is a slight bias in the recovery of the $\eta = \frac{1}{4}$ signal, so the two waveform models do not entirely agree in this limit.

Despite these discrepancies, the trend we have already seen in Figure 2 clearly persists in all cases: as the eccentricity of the signal increases, the recovered mass ratio becomes more consistent with that of a symmetric binary system. This is quite striking, particularly at $e_0 = 0.3$, the recovered mass ratio is consistent with an equal-mass binary, *regardless of the signal's mass ratio for all combinations of waveform models.*

3. Distance Estimates

From the representative corner plots of Figure 1, we can see that in eccentric case there is also a slight bias in the recovery of the luminosity distance. Figure 5 shows the trend for the case of a TEOBResumE signal with IMRPhenomD template. This overestimation of luminosity distance is consistent with the templates not capturing the entire signal SNR because of missing physical effects, i.e., orbital eccentricity. Having said that, even though there is a clear trend upward in the distance recovery, we find it to broadly remain within the statistical errors of the parameter estimation. We expect this bias to become significant only at even higher SNR than we consider. In the worst case, the median value is $\approx 50\%$ higher than that of the simulated value. We also note that the behavior is largely identical for each of the different simulations' mass ratio.

4. Maximum a-posteriori Estimated Waveforms

To help understand what features of the simulated and recovered best-fit waveforms contribute to the biases in parameter estimation, it is useful to look at the recovered maximum a posteriori (MAP) waveforms for some of our signals.

Figure 6 shows the maximum likelihood estimated IMRPhenomD waveform from four representative runs with $q = 0.33$, with TEOBResumE and ENIGMA-Inspiral used for the signals. There is strong agreement in the zero-

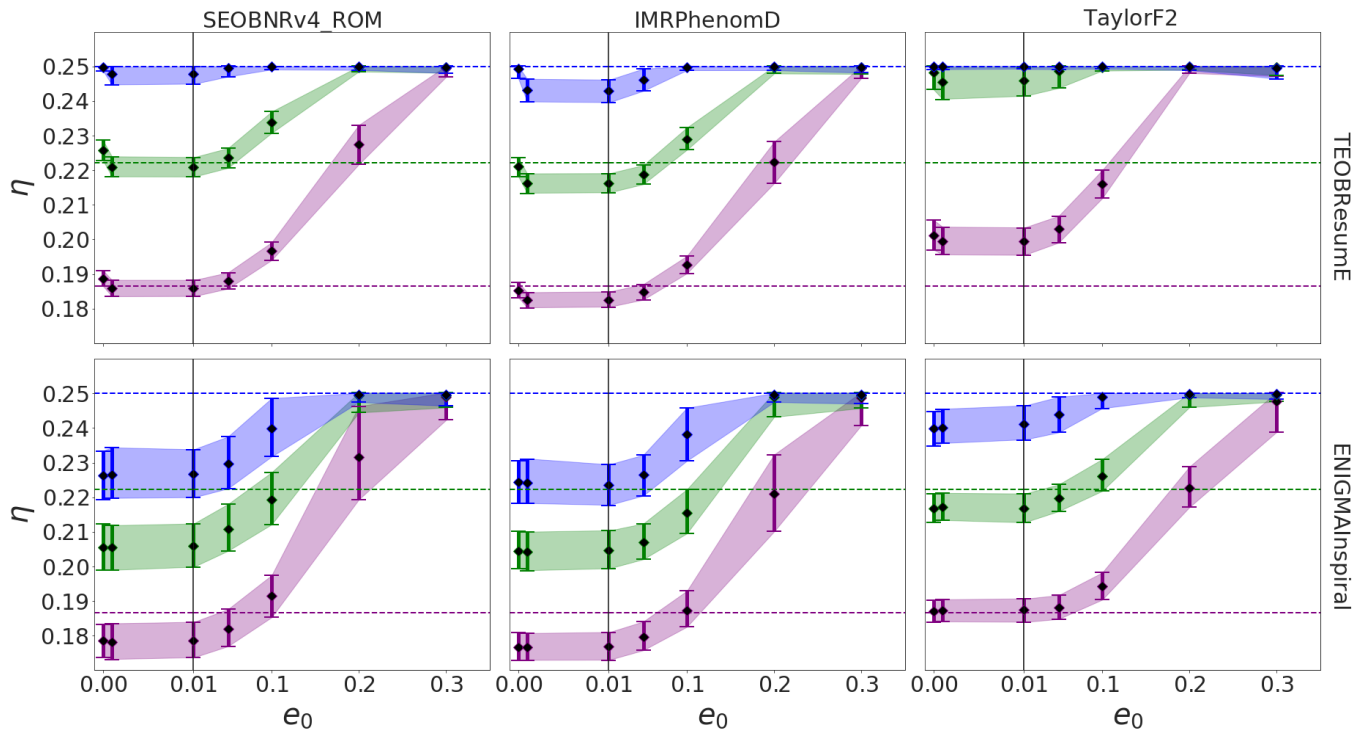


FIG. 4. Estimated values of the symmetric mass ratio for signals at different eccentricities. Dashed lines indicate the value of the simulated signal. The colors blue, green and purple correspond to the $q = 1, 0.5, 0.33$ signals respectively. The bars represent the 90% confidence intervals, with diamonds representing the median value. The shaded region is to illustrate the upward trend. The labels on top specify which model was used in the parameter estimation, and the labels on the right side of the figure specify which model was used to simulate the signal. Note the different scales between $[0., 0.01]$ and $[0.01, 0.3]$ on the x -axis.

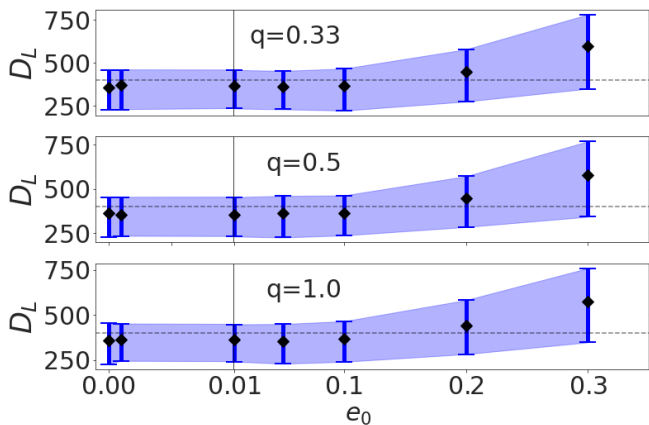


FIG. 5. Estimated values of the luminosity distance for varying eccentricity using TEOBResumE as the signal waveform and IMRPhenomD in the likelihood model. The dashed line is the signal's distance of 400 Mpc, with the bars represent the 90% confidence intervals, and diamonds the median value. Note the different scales between $[0., 0.01]$ and $[0.01, 0.3]$ on the x -axis.

eccentricity limit between the template and both signal waveform models, as is to be expected. When the eccentricity is increased to $e = 0.3$, the quasi-circular model

tries to best fit to the eccentric signal. In the case of the full IMR signal with TEOBResumE, the best quasi-circular template fits to the frequency of the *last few cycles* along with the merger-ringdown. In the inspiral-only case, the best template tries to fit to the *lower frequency cycles* of the last portion of the inspiral.

B. Gravitational-wave Events

Recently, Ref. [79] has indicated that two events GW151226 and G170608 in the first GW transients catalog [57] could be the mergers of eccentric binary black holes. This potentially overturned the conclusions of Ref. [41], which concluded that these two events were consistent with circular binary black hole mergers. An important difference between the two approaches was that the first used an inspiral-only, non-spinning waveform model [58], while the latter used a complete inspiral-merger-ringdown model from the effective-one-body family [61]. In the latter case, the posterior was not sampled directly since SEOBNRv4 is too expensive to evaluate, and the eccentric posteriors were found by reweighting the posteriors from non-eccentric runs.

In this section we study these two events with a two-fold purpose. We use the full IMR eccentric waveform

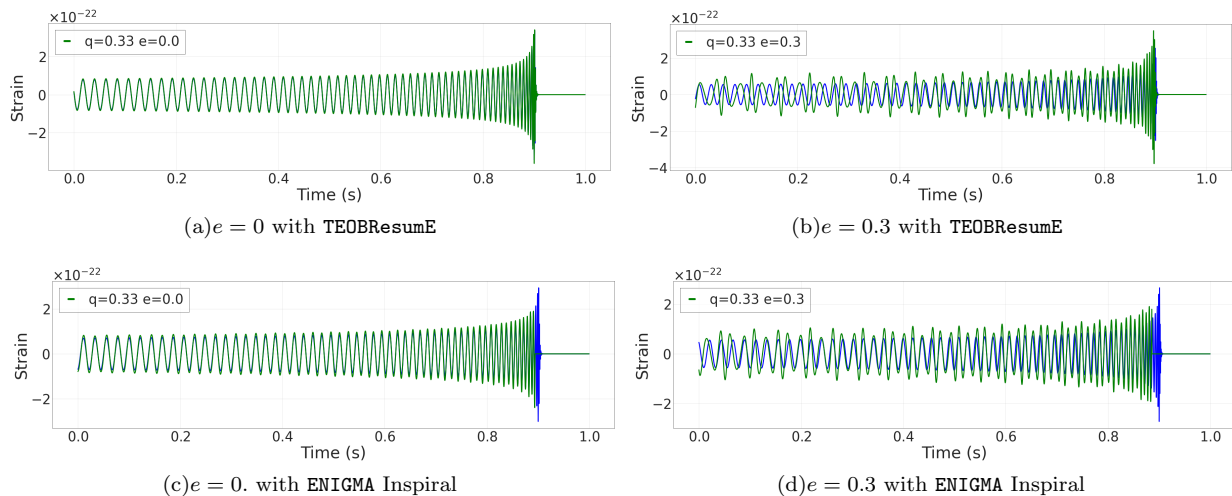


FIG. 6. Comparison of the maximum a posteriori **IMRPhenomD** waveform (blue) to the signal waveform (green) in the case of zero and non-zero eccentricity, with mass ratio $q = 0.33$. Only the last 1s of the waveform is shown and the coalescence time and phase of the waveforms have been aligned.

model to attempt to better understand the nature of these two events. And we use them to further confirm the measurement degeneracy between binary chirp mass and initial orbital eccentricity that we have so far shed light on using simulated signals. Our application of **TEOBResumE** is sufficiently fast to allow its direct use in parameter estimation runs with eccentricity and spins.

We use the same Bayesian inferencing setup as described in Sec. II B. We use the open-source data available from the Gravitational-Wave Open-Science Centre [73]. The estimated parameters with confidence intervals for this section are summarised in Table IV.

1. Non-spinning, Eccentric Inference

First we perform parameter estimation using **TEOBResumE** with a non-spinning prior, but now we include eccentricity in the analysis. Our prior for the eccentricity is uniform in the range $0 - 0.3$, and the waveforms are generated from a lower frequency of 10 Hz, rather than the 15 Hz used in our simulated signals. This is to allow us to compare our eccentricity measurements with Refs [41] and [42] who use this as their reference frequency. We again use $f_{min} = 20$ Hz in the evaluation of the likelihood integral in Eq. 3.

Panels (a) and (b) in Figure 7 show the parameter estimation results of these two events. In the case of GW151226 we measure an eccentricity of $e_0 \approx 0.2$, with $e_0 = 0$ strongly excluded from the posterior. Furthermore, in agreement with our study of simulated eccentric signals, the recovered chirp mass differs remarkably from that measured by the LVC in [73], by an amount greater than the statistical error of the measurement. In the case of GW170608, the recovered eccentricity is very much consistent with $e_0 = 0$. with an upper 90% estimate

of $e_0 = 0.16$. Its chirp mass is measured to be somewhat lower than the LVC estimate, albeit consistent with 90% credible intervals. In both cases the symmetric mass ratio is determined to be closer to $q = 1$ with greater certainty than the LVC estimate.

In both cases, the 2-dimensional marginalized posterior for the chirp mass and eccentricity corroborate what our simulated signal study found along with [43]: the measurement of the chirp mass and eccentricity are correlated. These results show that GW151226 is likely an eccentric system with a lower chirp mass than previously thought, if we can disregard component spins. The same effect is observed to a lesser degree in GW170608, which we find to be consistent with having a non-eccentric origin. We also note that allowing for eccentricity as a degree of freedom helps narrow down the measurement of both chirp mass and mass ratio for this event.

2. The importance of including spin

It is well known that the measurement of binary spins is correlated with the measurement of the mass parameters when determining the source parameters of gravitational-wave signals. As explained by [80], the error in the estimated chirp mass and mass ratio increase when one includes the spins of compact objects in their analysis, even if the system is non-spinning. This makes it reasonable to expect our confident mass estimates to be influenced by the exclusion of spin in our prior. Also, as we have found previously, the chirp mass measurement is correlated with orbital eccentricity, and so it is also possible that the chirp mass measurement is correlated with the spin measurement.

We repeat our analysis of the two events GW151226 and GW170608, with the same set of priors as in the

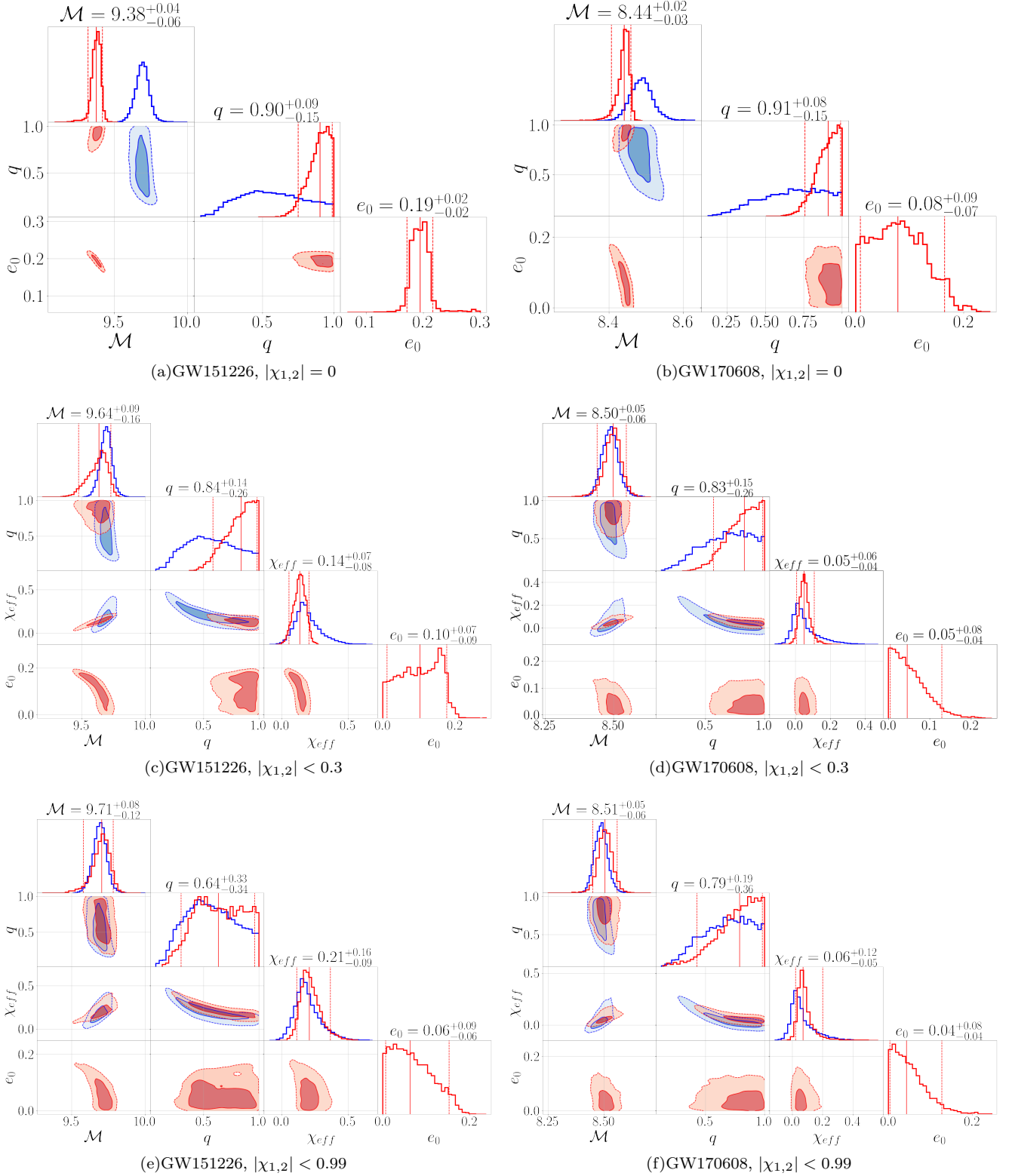


FIG. 7. *Red*: Posterior probability distribution using TEOBResumE with a for GW151226 and GW170608 with an eccentric prior. Indicated is the maximum value of the z -component of the spin, χ , allowed in the prior. Median estimates with 90% confidence intervals are shown for this data. *Blue*: GWTC-2 data from [78]. Contours show the regions of 50% and 90% confidence. See Table IV for a comparison with the exact medians and error estimates of the GWTC data.

previous section, but now with an aligned-spin prior. We use the “z-prior” implemented in Bilby and described in [81] for the aligned spins. We perform several runs with different values of the maximum spin magnitude for the prior to investigate how the resulting posterior depends on the spin prior. We use $|\chi_{\max}| < 0.3, 0.7, 0.99$. The value of 0.7 is chosen since the model `TEOBResumE` is only validated against NR waveforms with spin up to this value. In the results we will quote only the results of the effective spin, which is the best recovered spin parameter [82] and is defined as

$$\chi_{\text{eff}} = \frac{m_1\chi_1 + m_2\chi_2}{M} \quad (5)$$

where M is the total mass and $\chi_{1,2}$ are the components of the spin aligned with the binary’s orbital angular momentum.

Panels (c) and (d) in Figure 7 show the results for the two events with $|\chi_{1,2}| < 0.3$. Panel (c) shows the results from GW151226. The posterior for eccentricity now has support for $e_0 = 0$, in contrast with the non-spinning prior, although the e_0 posterior peaks at about $e_0 = 0.16$. From the $\mathcal{M}_c - e_0$ plane, we can clearly see the negative correlation between the chirp mass and eccentricity. The chirp mass estimate agrees better with that of the LVC than in the non-spinning case, except the posterior is slightly broader due to the higher eccentricity contribution of the posterior. Most interesting for this event is the $\chi_{\text{eff}} - e_0$ plane: we see a negative correlation between the spin and eccentricity measurements, with $e_0 = \chi_{\text{eff}} = 0$ excluded.

Panel (d) of Figure 7 shows the results for GW170608. We find that including spins has much improved the agreement with the LVC chirp mass estimate. Also the posterior for orbital eccentricity has become narrower, with the upper 90% credible limit decreasing from $e_0 = 0.18$ to 0.13. We can conclude that even when the event being analysed is likely non-eccentric, including spin in the analysis improves the confidence in the eccentricity constraints.

Panels (e) and (f) show the results from expanding the maximum spin in the prior to 0.99. Panel (e) shows the event GW151226. We can immediately see that the constraint on the eccentricity is improved, and the recovery of the masses and effective spin are in better agreement with the GWTC-2 values. The correlation between the effective spin and eccentricity is still present in the 2D $\chi_{\text{eff}} - e_0$ posterior but appears weaker than in the case of the restricted spin prior. This demonstrates further that the measurement of the eccentricity is correlated with that of the spin, and that to accurately measure the eccentricity one should sample from as much of the spin prior as possible, which requires waveform models that are reliable for moderate to large spin values.

Panel (f) shows the event GW170608. In this case the posteriors are largely unchanged from the $|\chi_{1,2}| < 0.3$ case, with the eccentricity constraint becoming $e_0 < 0.12$. Since this event does not have appreciable spin, the more

Prior	GW151226	GW170608
$ \chi_{1,2} < 0.3$	0.81	0.28
$ \chi_{1,2} < 0.7$	0.45	0.28
$ \chi_{1,2} < 0.99$	0.40	0.28

TABLE III. Bayes factors for the eccentric versus non-eccentric model, with increasing value of the maximum spin in the prior.

restrictive spin prior is well able to account for the full range of physics contributing to the posterior.

Table IV summarises the results from each of our runs. We opt not to plot the posteriors for the case of $|\chi_{1,2}| < 0.7$ but the results are largely unchanged between this case and that of $|\chi_{1,2}| < 0.99$, despite the `TEOBResumE` model not being validated to spins of that magnitude.

To evaluate the preference for the eccentric model over the non-eccentric one, we can calculate the Bayes factor:

$$\mathcal{B} = \frac{Z_{\text{eccentric}}}{Z_{\text{non-eccentric}}}. \quad (6)$$

where Z is the Bayesian evidence. Since the set of parameters for the non-eccentric model is nested within the full eccentric model, this ratio becomes the Savage-Dickey factor [83]:

$$\mathcal{B} = \frac{\pi(e_0 = 0)}{p(e_0 = 0)} \quad (7)$$

which is simply the ratio of value of the prior weight $\pi(e_0 = 0)$ to the posterior weight $p(e_0 = 0)$.

Table III shows the estimated Bayes’ factors for the two events as a function of increasing the maximum in the spin prior. In all cases we have $\mathcal{B} < 1$, indicating that the non-eccentric model is preferred. In the case of GW151226, the preference for the non-eccentric model increases as the maximum spin is increased in the prior. As expected from our previous results, increasing the spin has little effect on the results in the case of GW170608.

C. Circular Simulated Signals for GW151226 and GW17060

We reaffirm our findings for GW151226 and GW170608 by follow-up analyses with a set of simulated signal studies. The purpose of this is to investigate how binary source parameters would be recovered using `TEOBResumE`, if the signals were truly non-eccentric. We use the MAP source parameters from the GWTC posteriors for GW170608 and GW151226, and again inject the signals into zero-noise, and use the LIGO Hanford and Livingston detectors noise curves.

We use the `TEOBResumE` model with aligned spins to simulate the signals, and then repeat our parameter estimation using the same model, with the sampler setup from our previous runs. We wish for the signal to have

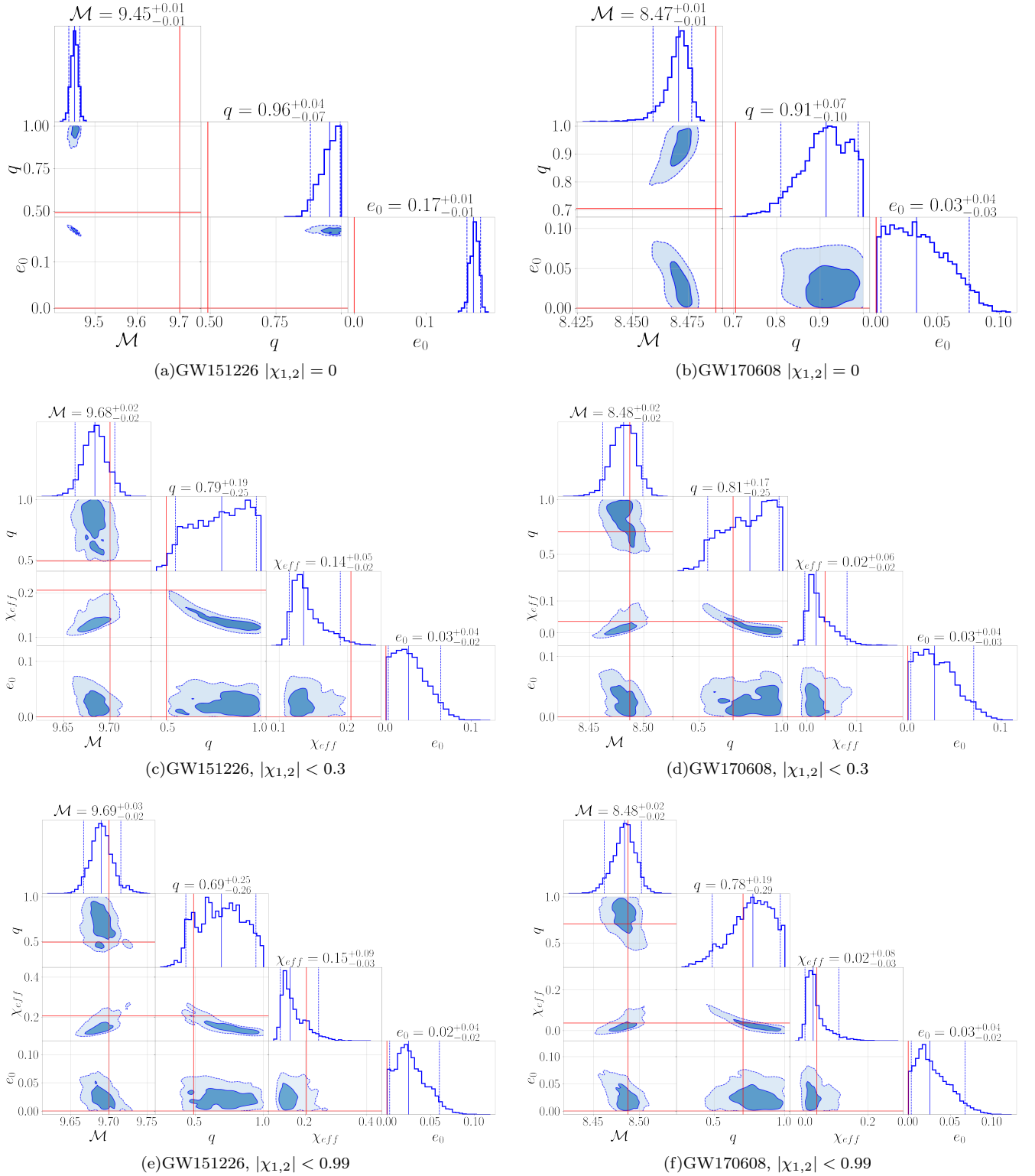


FIG. 8. Posterior probability distributions for the chirp mass, \mathcal{M} , mass ratio q , effective spin χ_{eff} and eccentricity e_0 , recovered using TEOBResumE. Red marks the simulated signal's values, which correspond to the MAP values given by the GWTC posteriors for each event. Shaded contours correspond to the 90% and 50% confidence regions.

$e_0 = 0$, but from Figure 4 we saw that **TEOBResumE** has a discontinuity at $e_0 = 0$ so we set the value to 10^{-10} . We generate our signals from a lower frequency of 10 Hz, and use 20 Hz as the lower frequency cutoff in the evaluation of the likelihood integral. We use the same eccentricity prior as before in all cases, and again perform two runs for each event’s parameters: with a non-spinning prior and with an aligned spin prior.

Figure 8 shows the results for the two events’ parameters using both a non-spinning and an aligned-spin prior with $\chi_{1,2} < 0.3$ and < 0.99 . Panels (a) and (b) show the non-spinning case. We see the same general trends as in Figure 7 with the real event data: the chirp mass for both events is underestimated, the mass ratio is overestimated to be more consistent with that of a symmetric binary, and the presence of spin in the case of GW151226 leads to a spurious eccentricity measurement.

Panels (c) and (d) shows the results when the prior is expanded to include aligned spins up to 0.3. Since we are using the same waveform model for the signal and the parameter estimation, we now see a much better recovery of parameters as expected. Again the non-zero eccentricity measurement for GW151226 disappears.

In particular, the correlation between spin and eccentricity seen in panels (c) and (e) in Figure 7 is not seen, and the signal is well recovered as a spinning non-eccentric signal.

Panels (e) and (f) show the results when the maximum spin is increased to 0.99. The results are qualitatively similar, but the recovery of the effective spin is improved.

These results also further illustrate the fact the mass parameters, spin and eccentricity are all correlated and it is important to include each of these effects when performing parameter estimation. We defer a more systematic investigation of this degeneracy to future work.

IV. DISCUSSION

Let’s consider a single case from our simulated signal recovery, with $M_{\text{total}}^{\text{signal}} = 20M_{\odot}$ and $q^{\text{signal}} = 0.33$. This corresponds to $m_1^{\text{signal}} \approx 15M_{\odot}$ and $m_2^{\text{signal}} \approx 5M_{\odot}$, but the recovered source masses would be $m_1 \approx m_2 \approx 9.2M_{\odot}$. Correct inference of the source masses is important for our understanding of the population of such objects, and in extreme cases such biases could be enough to incorrectly identify certain objects to inside or outside of the NS-BH mass gap of $\approx 2 - 5M_{\odot}$ or the supernova pair-instability mass gap of $\gtrsim 50M_{\odot}$. Thus, determining whether a signal is eccentric is important for the determination of the rest of its source parameters. As more detectors join the array of ground based detectors, the SNR of such eccentric signals will increase and systematic biases will become more pronounced when compared to the estimated error from the parameter estimation.

In section IIIB and IIIC we could see the $\mathcal{M}_c - e_0$ correlation manifest in the 2-D marginalized posterior for the two gravitational wave events GW151226 and

TABLE IV. Median estimates of source parameters from using **TEOBResumE** for parameter estimation. The left-hand column specifies the prior on the aligned spin, or whether the data is from GWTC-2. Upper and lower error estimates are the 90% confidence intervals of the 1D marginalized posterior.

	\mathcal{M}_c	q	χ_{eff}	e_0
GW151226				
$ \chi_{1,2} = 0$	$9.38_{-0.06}^{+0.04}$	$0.90_{-0.15}^{+0.09}$	—	$0.19_{-0.02}^{+0.02}$
$ \chi_{1,2} \leq 0.3$	$9.64_{-0.16}^{+0.09}$	$0.84_{-0.26}^{+0.14}$	$0.14_{-0.08}^{+0.07}$	$0.10_{-0.09}^{+0.07}$
$ \chi_{1,2} \leq 0.7$	$9.70_{-0.12}^{+0.08}$	$0.68_{-0.37}^{+0.29}$	$0.20_{-0.09}^{+0.15}$	$0.6_{-0.06}^{+0.09}$
$ \chi_{1,2} \leq 0.99$	$9.71_{-0.12}^{+0.08}$	$0.64_{-0.34}^{+0.33}$	$0.21_{-0.09}^{+0.6}$	$0.6_{-0.06}^{+0.09}$
GWTC-2:	$9.69_{-0.06}^{+0.08}$	$0.56_{-0.23}^{+0.38}$	$0.18_{-0.12}^{+0.20}$	—
GW170608				
$ \chi_{1,2} = 0$	$8.44_{-0.03}^{+0.02}$	$0.91_{-0.15}^{+0.08}$	—	$0.08_{-0.07}^{+0.08}$
$ \chi_{1,2} \leq 0.3$	$8.50_{-0.06}^{+0.05}$	$0.83_{-0.26}^{+0.15}$	$0.05_{-0.04}^{+0.06}$	$0.05_{-0.04}^{+0.08}$
$ \chi_{1,2} \leq 0.7$	$8.50_{-0.5}^{+0.05}$	$0.79_{-0.34}^{+0.19}$	$0.06_{-0.05}^{+0.11}$	$0.04_{-0.04}^{+0.08}$
$ \chi_{1,2} \leq 0.99$	$8.51_{-0.6}^{+0.05}$	$0.79_{-0.36}^{+0.19}$	$0.06_{-0.05}^{+0.12}$	$0.04_{-0.04}^{+0.08}$
GWTC-2:	$8.49_{-0.05}^{+0.05}$	$0.69_{-0.36}^{+0.28}$	$0.03_{-0.06}^{+0.18}$	—

GW170608. Although performing inference on these events with a non-spinning, eccentric prior corroborated this correlation, neglecting to include spin in the analysis leads to over-confident and biased estimates of the mass parameters. Clearly a more systematic investigation of the relation effects of eccentricity on the spin measurement and vice-versa are needed, which we defer to a future study.

In future we will want to accurately measure the eccentricities of newly detected signals, as well as those already present in GWTC2. It is clear that we will not only need accurate and fast-to-evaluate waveform models that can incorporate eccentricity, but also spins, and most likely precession. By using, **TEOBResumE** we have constrained the eccentricities of GW170608 and GW151226 to be < 0.12 and 0.15 at 90% confidence respectively. Our constraints are slightly tighter than the values of < 0.166 and < 0.181 found by [42] which used a non-spinning, inspiral-only model. However, we find a much looser constraint than those set by Ref. [41], which found $e_0 < 0.04$ for each of these events by re-weighting samples from a non-eccentric parameter estimation run using the model **SEOBRE**. From Fig 8, we found that our method could only constrain a zero eccentricity to about $e_0 \approx 0.06$. In a similar light Ref [43] also found that their measurement of the eccentricity of GW190425 is a much looser constraint than that of Ref. [41], and explains that this could be due

to the use of a log-uniform prior on e_0 , but also that the application of posterior re-weighting scheme might have failed to capture the correlations *between the chirp mass and eccentricity*, leading to overconfident measurements as compared to their full MCMC calculation (although one does find a hint of the correlation between eccentricity in the supplementary figures [84, 85] of Ref. [41], making the difference in priors a more likely explanation). One way to compare posteriors which use different priors is to use rejection sampling to reweight the posterior from one prior to another. However, we found that the reweighting efficiency from a uniform to log-uniform prior is too low and results in only ≈ 40 samples from the initial ≈ 20000 samples. To fully investigate the choice of prior thus requires performing the parameter estimation with a log-uniform prior, which we defer to a future study.

In this paper we chose to focus on the two lower mass black hole events from the GWTC1 data. It would be interesting to continue this analysis by applying `TEOBResumE` to the parameter estimation of the rest of GWTC-2, in particular to see whether the eccentricity of events such as GW190521 can be established or further constrained, and also whether the presence of eccentricity has biased the existing LVC estimates of their source parameters.

V. SUMMARY

In section III A we showed that there is correlation between the measurement of the mass parameters of a binary compact object system and its eccentricity. If one uses quasi-circular templates in their parameter estimation, this correlation manifests as a bias in the measured chirp mass and mass ratio. In the moderately eccentric case of $e = 0.3$, a bias in the chirp mass of up to $\approx 4\%$ can occur, but the bias in the mass ratio can be much more, since it tends to make the binary system appear more symmetric.

In section III B we sought to further establish this correlation on real gravitational wave data. However, we found that in order to correctly estimate the masses along with the eccentricity of such systems, we must employ a waveform model that can account for eccentricity and spins simultaneously.

By using the eccentric, aligned spin model `TEOBResumE`, we measured the eccentricity of GW170608 and GW151226 to be < 0.12 and 0.15 at 90% confidence respectively.

ACKNOWLEDGMENTS

We thank Alessandro Nagar for instructions on using the implementation of the `TEOBResumE` model [86], and Antoni Ramos Buades for helpful comments. The

authors gratefully acknowledge the NSF Grants PHY-1912081 and OAC-193128 and a grant from the Sherman Fairchild Foundation at Cornell. P.K.'s research was also supported by the Department of Atomic Energy, Government of India, and by the Ashok and Gita Vaish Early Career Faculty Fellowship at the International Centre for Theoretical Sciences. The authors are grateful for computational resources provided by the LIGO Laboratory and supported by National Science Foundation Grants PHY-0757058 and PHY-0823459.

Appendix A: ENIGMA Merger-ringdown

The merger-ringdown portion of the ENIGMA waveform is constructed under the assumption that a moderately eccentric compact binary has circularized by the time it has reached merger, which has been shown to occur in numerical relativity simulations of eccentric binaries [87]. Under this assumption, the parameter space for the merger-ringdown portion of the waveform becomes one-dimensional, depending only on the mass ratio q . A one-dimensional Gaussian-process-regression surrogate model is constructed to interpolate between a training set of quasi-circular numerical relativity waveforms to any mass ratio up to $q = 10$.

The final step in generating an ENIGMA waveform is finding the optimal attachment time between the PN inspiral waveform and the surrogate merger-ringdown waveform. The optimal attachment frequency is determined to be that which optimizes the overlap between a circular ENIGMA waveform and the corresponding `SEOBNRv4` waveform. This overlap is calculated as in equation 4 with $f_{min} = 15$ Hz and $f_{max} = 4096$ Hz. Due to the instantaneous monochromaticity of these circular waveforms, the attachment frequency can be converted to a corresponding attachment time.

In our studies, we found that ENIGMA sometimes furnishes qualitatively incorrect waveforms at smaller values of total mass, and mass ratios < 0.5 . This is because the optimal matching time is found by optimizing the overlap of two waveforms, but with respect to the LIGO PSD. At lower masses, which correspond to higher gravi-

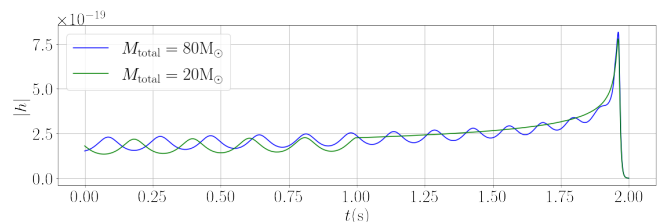


FIG. 9. *Green*: Amplitude of ENIGMA generated waveform with $m_1 = 14M_\odot$, $m_2 = 6M_\odot$, $e_0 = 0.3$. *Blue*: The ENIGMA generated waveform with the masses scaled by a factor of 4. The amplitude and samples times of the waveform are scaled by the same factor of 4 so they can be compared.

tational wave frequencies, the LIGO PSD pushes the optimum attachment frequency lower than it should. The attachment time is then many cycles before the merger, and the assumption that the eccentricity has radiated before attaching the merger-ringdown waveform is no longer valid. This manifests as a cusp in the amplitude of the waveform. Figure 9 illustrates the difference be-

tween ENIGMA-generated waveforms with $M_{\text{total}} = 20M_{\odot}$ and $M_{\text{total}} = 80M_{\odot}$. The rescaled amplitudes should be coincident, but in the low mass case the eccentricity "switches off" in a non-smooth manner many cycles before the merger. We find this same behavior regardless of the eccentricity value, but have chosen $e_0 = 0.3$ to accentuate the modulation of the amplitude and make the difference more visible.

-
- [1] R. A. et. al, "Gwtc-2: Compact binary coalescences observed by ligo and virgo during the first half of the third observing run," (2020), arXiv:2010.14527 [gr-qc].
- [2] Nature Astronomy **3**, 35–40 (2019).
- [3] C. S. Unnikrishnan, International Journal of Modern Physics D **22**, 1341010 (2013).
- [4] D. Reitze, R. X. Adhikari, S. Ballmer, B. Barish, L. Barsotti, G. Billingsley, D. A. Brown, Y. Chen, D. Coyne, R. Eisenstein, M. Evans, P. Fritschel, E. D. Hall, A. Lazzarini, G. Lovelace, J. Read, B. S. Sathyaprakash, D. Shoemaker, J. Smith, C. Torrie, S. Vitale, R. Weiss, C. Wipf, and M. Zucker, "Cosmic explorer: The u.s. contribution to gravitational-wave astronomy beyond ligo," (2019), arXiv:1907.04833 [astro-ph.IM].
- [5] M. Maggiore, C. V. D. Broeck, N. Bartolo, E. Belgacem, D. Bertacca, M. A. Bizouard, M. Branchesi, S. Clesse, S. Foffa, J. García-Bellido, and et al., Journal of Cosmology and Astroparticle Physics **2020**, 050–050 (2020).
- [6] B. P. Abbott *et al.* (LIGO Scientific, Virgo), Astrophys. J. Lett. **818**, L22 (2016), arXiv:1602.03846 [astro-ph.HE].
- [7] P. Marchant, K. M. W. Pappas, M. Gallegos-Garcia, C. P. L. Berry, R. E. Taam, V. Kalogera, and P. Podsiadlowski, "The role of mass transfer and common envelope evolution in the formation of merging binary black holes," (2021), arXiv:2103.09243 [astro-ph.SR].
- [8] J. J. Andrews, J. Cronin, V. Kalogera, C. Berry, and A. Zezas, "Targeted modeling of gw150914's binary black hole source with dartboard," (2020), arXiv:2011.13918 [astro-ph.HE].
- [9] M. Zevin, S. S. Bavera, C. P. L. Berry, V. Kalogera, T. Fragos, P. Marchant, C. L. Rodriguez, F. Antonini, D. E. Holz, and C. Pankow, The Astrophysical Journal **910**, 152 (2021).
- [10] N. Ivanova, S. Justham, X. Chen, O. De Marco, C. L. Fryer, E. Gaburov, H. Ge, E. Glebbeek, Z. Han, X.-D. Li, and et al., The Astronomy and Astrophysics Review **21** (2013), 10.1007/s00159-013-0059-2.
- [11] M. Livio and N. Soker, Astrophys. J. **329**, 764 (1988).
- [12] Kruckow, M. U., Tauris, T. M., Langer, N., Szécsi, D., Marchant, P., and Podsiadlowski, Ph., A&A **596**, A58 (2016).
- [13] S. E. de Mink, M. Cantiello, N. Langer, O. R. Pols, V. Kalogera, and M. van der Sluys, (2010), 10.1063/1.3536387.
- [14] S. E. de Mink and I. Mandel, Monthly Notices of the Royal Astronomical Society **460**, 3545–3553 (2016).
- [15] M. Zevin, C. Pankow, C. L. Rodriguez, L. Sampson, E. Chase, V. Kalogera, and F. A. Rasio, The Astrophysical Journal **846**, 82 (2017).
- [16] S. F. P. Zwart and S. L. W. McMillan, The Astrophysical Journal **528**, L17 (2000).
- [17] C. L. Rodriguez, M. Morscher, B. Pattabiraman, S. Chatterjee, C.-J. Haster, and F. A. Rasio, Physical Review Letters **115** (2015), 10.1103/physrevlett.115.051101.
- [18] C. L. Rodriguez, M. Zevin, C. Pankow, V. Kalogera, and F. A. Rasio, The Astrophysical Journal **832**, L2 (2016).
- [19] C. L. Rodriguez, C.-J. Haster, S. Chatterjee, V. Kalogera, and F. A. Rasio, The Astrophysical Journal **824**, L8 (2016).
- [20] R. M. O’Leary, Y. Meiron, and B. Kocsis, The Astrophysical Journal **824**, L12 (2016).
- [21] Y. Yang, I. Bartos, Z. Haiman, B. Kocsis, Z. Márka, N. C. Stone, and S. Márka, The Astrophysical Journal **876**, 122 (2019).
- [22] B. McKernan, K. E. S. Ford, and R. O’Shaughnessy, Monthly Notices of the Royal Astronomical Society **498**, 4088–4094 (2020).
- [23] M. Gröbner, W. Ishibashi, S. Tiwari, M. Haney, and P. Jetzer, Astronomy & Astrophysics **638**, A119 (2020).
- [24] D. Gerosa and E. Berti, Phys. Rev. D **95**, 124046 (2017).
- [25] C. L. Rodriguez, M. Zevin, P. Amaro-Seoane, S. Chatterjee, K. Kremer, F. A. Rasio, and C. S. Ye, Phys. Rev. D **100** (2019), 10.1103/physrevd.100.043027.
- [26] S. E. Woosley, The Astrophysical Journal **878**, 49 (2019).
- [27] S. E. Woosley, The Astrophysical Journal **836**, 244 (2017).
- [28] C. Talbot and E. Thrane, Phys. Rev. D **96**, 023012 (2017).
- [29] C. L. Rodriguez, P. Amaro-Seoane, S. Chatterjee, K. Kremer, F. A. Rasio, J. Samsing, C. S. Ye, and M. Zevin, Phys. Rev. D **98**, 123005 (2018).
- [30] J. Samsing, D. J. D’Orazio, A. Askar, and M. Giersz, "Black hole mergers from globular clusters observable by lisa and ligo: Results from post-newtonian binary-single scatterings," (2018), arXiv:1802.08654 [astro-ph.HE].
- [31] M. Zevin, J. Samsing, C. Rodriguez, C.-J. Haster, and E. Ramirez-Ruiz, The Astrophysical Journal **871**, 91 (2019).
- [32] M. L. Lidov, Planetary and Space Science **9**, 719 (1962).
- [33] Y. Kozai, The Astronomical Journal **67**, 591 (1962).
- [34] J. Samsing, Phys. Rev. D **97**, 103014 (2018).
- [35] C. L. Rodriguez, P. Amaro-Seoane, S. Chatterjee, and F. A. Rasio, Phys. Rev. Lett. **120**, 151101 (2018).
- [36] H. Tagawa, B. Kocsis, Z. Haiman, I. Bartos, K. Omukai, and J. Samsing, The Astrophysical Journal **907**, L20 (2021).
- [37] J. Samsing, I. Bartos, D. J. D’Orazio, Z. Haiman, B. Kocsis, N. W. C. Leigh, B. Liu, M. E. Pessah, and H. Tagawa, "Active galactic nuclei as factories for eccentric black hole mergers," (2020), arXiv:2010.09765 [astro-ph.HE].
- [38] B. P. Abbott *et al.* (LIGO Scientific, Virgo), Astrophys.

- J. **883**, 149 (2019), arXiv:1907.09384 [astro-ph.HE].
- [39] R. Abbott *et al.* (LIGO Scientific, Virgo), *Astrophys. J. Lett.* **900**, L13 (2020), arXiv:2009.01190 [astro-ph.HE].
- [40] A. H. Nitz, A. Lenon, and D. A. Brown, *The Astrophysical Journal* **890**, 1 (2020).
- [41] I. M. Romero-Shaw, P. D. Lasky, and E. Thrane, *Monthly Notices of the Royal Astronomical Society* **490**, 5210–5216 (2019).
- [42] S. Wu, Z. Cao, and Z.-H. Zhu, *Monthly Notices of the Royal Astronomical Society* **495**, 466–478 (2020).
- [43] A. K. Lenon, A. H. Nitz, and D. A. Brown, *Monthly Notices of the Royal Astronomical Society* **497**, 1966–1971 (2020).
- [44] C. Kimball, C. Talbot, C. P. L. Berry, M. Zevin, E. Thrane, V. Kalogera, R. Buscicchio, M. Carney, T. Dent, H. Middleton, E. Payne, J. Veitch, and D. Williams, “Evidence for hierarchical black hole mergers in the second ligo–virgo gravitational-wave catalog,” (2020), arXiv:2011.05332 [astro-ph.HE].
- [45] R. Gamba, M. Breschi, G. Carullo, P. Rettengo, S. Albanesi, S. Bernuzzi, and A. Nagar, (2021), arXiv:2106.05575 [gr-qc].
- [46] V. Gayathri, J. Healy, J. Lange, B. O’Brien, M. Szczepanczyk, I. Bartos, M. Campanelli, S. Klimentko, C. Lousto, and R. O’Shaughnessy, “Gw190521 as a highly eccentric black hole merger,” (2020), arXiv:2009.05461 [astro-ph.HE].
- [47] I. M. Romero-Shaw, P. D. Lasky, E. Thrane, and J. C. Bustillo, (2020), arXiv:2009.04771.
- [48] S. Sato, S. Kawamura, M. Ando, T. Nakamura, K. Tsubono, A. Araya, I. Funaki, K. Ioka, N. Kanda, S. Moriwaki, M. Musha, K. Nakazawa, K. Numata, S. ichiro Sakai, N. Seto, T. Takashima, T. Tanaka, K. Agatsuma, K. suke Aoyanagi, K. Arai, H. Asada, Y. Aso, T. Chiba, T. Ebisuzaki, Y. Ejiri, M. Enoki, Y. Eriguchi, M.-K. Fujimoto, R. Fujita, M. Fukushima, T. Futamase, K. Ganzu, T. Harada, T. Hashimoto, K. Hayama, W. Hikida, Y. Himemoto, H. Hirabayashi, T. Hiramatsu, F.-L. Hong, H. Horisawa, M. Hosokawa, K. Ichiki, T. Ikegami, K. T. Inoue, K. Ishidoshiro, H. Ishihara, T. Ishikawa, H. Ishizaki, H. Ito, Y. Itoh, N. Kawashima, F. Kawazoe, N. Kishimoto, K. Kiuchi, S. Kobayashi, K. Kohri, H. Koizumi, Y. Kojima, K. Kokeyama, W. Kokuyama, K. Kotake, Y. Kozai, H. Kudoh, H. Kunimori, H. Kuminaka, K. Kuroda, K. ichi Maeda, H. Matsuhara, Y. Mino, O. Miyakawa, S. Miyoki, M. Y. Morimoto, T. Morioka, T. Morisawa, S. Mukohyama, S. Nagano, I. Naito, K. Nakamura, H. Nakano, K. Nakao, S. Nakasuka, Y. Nakayama, E. Nishida, K. Nishiyama, A. Nishizawa, Y. Niwa, T. Noumi, Y. Obuchi, M. Ohashi, N. Ohishi, M. Ohkawa, N. Okada, K. Onozato, K. Oohara, N. Sago, M. Saijo, M. Sakagami, S. Sakata, M. Sasaki, T. Sato, M. Shibata, H. Shinkai, K. Somiya, H. Sotani, N. Sugiyama, Y. Suwa, R. Suzuki, H. Tagoshi, F. Takahashi, K. Takahashi, K. Takahashi, R. Takahashi, R. Takahashi, T. Takahashi, H. Takahashi, T. Akiteru, T. Takano, K. Taniguchi, A. Taruya, H. Tashiro, Y. Torii, M. Toyoshima, S. Tsujikawa, Y. Tsunesada, A. Ueda, K. ichi Ueda, M. Utashima, Y. Wakabayashi, H. Yamakawa, K. Yamamoto, T. Yamazaki, J. Yokoyama, C.-M. Yoo, S. Yoshida, and T. Yoshino, *Journal of Physics: Conference Series* **840**, 012010 (2017).
- [49] S. Kawamura *et al.*, (2020), arXiv:2006.13545 [gr-qc].
- [50] Z. Chen, E. A. Huerta, J. Adamo, R. Haas, E. O’Shea, P. Kumar, and C. Moore, “Observation of eccentric binary black hole mergers with second and third generation gravitational wave detector networks,” (2020), arXiv:2008.03313 [gr-qc].
- [51] V. Tiwari, S. Klimentko, N. Christensen, E. A. Huerta, S. R. Mohapatra, A. Gopakumar, M. Haney, P. Ajith, S. T. McWilliams, G. Vedovato, M. Drago, F. Salemi, G. A. Prodi, C. Lazzaro, S. Tiwari, G. Mitselmakher, and F. Da Silva, *Phys. Rev. D* **93** (2016), 10.1103/PhysRevD.93.043007.
- [52] E. A. Huerta and D. A. Brown, *Phys. Rev. D* **87** (2013), 10.1103/physrevd.87.127501.
- [53] E. A. Huerta, C. J. Moore, P. Kumar, D. George, A. J. K. Chua, R. Haas, E. Wessel, D. Johnson, D. Glennon, A. Rebei, A. M. Holgado, J. R. Gair, and H. P. Pfeiffer, *Phys. Rev. D* **97** (2017), 10.1103/PhysRevD.97.024031, 1711.06276.
- [54] P. C. Peters and J. Mathews, *Phys. Rev.* **131**, 435 (1963).
- [55] K. Martel and E. Poisson, *Phys. Rev. D* **60** (1999), 10.1103/physrevd.60.124008.
- [56] B. P. Abbott *et al.* (LIGO Scientific, Virgo), *Class. Quant. Grav.* **34**, 104002 (2017), arXiv:1611.07531 [gr-qc].
- [57] B. Abbott, R. Abbott, T. Abbott, S. Abraham, F. Acernese, K. Ackley, C. Adams, R. Adhikari, V. Adya, C. Affeldt, and et al., *Phys. Rev. X* **9** (2019), 10.1103/physrevx.9.031040.
- [58] E. A. Huerta, P. Kumar, S. T. McWilliams, R. O’Shaughnessy, and N. Yunes, *Phys. Rev. D* **90**, 084016 (2014).
- [59] S. Tanay, M. Haney, and A. Gopakumar, *Phys. Rev. D* **93**, 064031 (2016).
- [60] LIGO Scientific Collaboration, “LIGO Algorithm Library - LALSuite,” free software (GPL) (2018).
- [61] Z. Cao and W.-B. Han, *Phys. Rev. D* **96**, 044028 (2017).
- [62] D. Chiaramello and A. Nagar, *Phys. Rev. D* **101** (2020), 10.1103/PhysRevD.101.101501, arXiv:2001.11736.
- [63] T. Islam, V. Varma, J. Lodman, S. E. Field, G. Khanna, M. A. Scheel, H. P. Pfeiffer, D. Gerosa, and L. E. Kidder, *Phys. Rev. D* **103** (2021), 10.1103/physrevd.103.064022.
- [64] A. Nagar, G. Pratten, G. Riemenschneider, and R. Gamba, *Phys. Rev. D* **101**, 024041 (2020).
- [65] D. Chiaramello and A. Nagar, *Phys. Rev. D* **101** (2020), 10.1103/physrevd.101.101501.
- [66] “TEOBResumS: Effective-one-body model with spin and tidal interactions,” https://bitbucket.org/eob_ihes/teobresums/src/master/ (2021).
- [67] G. Ashton, M. Hübner, P. D. Lasky, C. Talbot, K. Ackley, S. Biscoveanu, Q. Chu, A. Divakarla, P. J. Easter, B. Goncharov, F. Hernandez Vivanco, J. Harms, M. E. Lower, G. D. Meadors, D. Melchor, E. Payne, M. D. Pitkin, J. Powell, N. Sarin, R. J. E. Smith, and E. Thrane, *ApJS* **241**, 27 (2019), arXiv:1811.02042 [astro-ph.IM].
- [68] “Advanced ligo anticipated sensitivity curves,” <https://dcc.ligo.org/LIGO-T0900288/public>.
- [69] J. S. Speagle, *Monthly Notices of the Royal Astronomical Society* **493**, 3132–3158 (2020).
- [70] W. Farr, “Marginalisation of the time parameter in gravitational wave parameter estimation,” <https://dcc.ligo.org/T1400460-v2/public>.
- [71] J. Veitch and W. Del Pozzo, “Analytic marginalisation of phase parameter,” <https://dcc.ligo.org/>

- LIGO-T1300326/public.
- [72] E. Thrane and C. Talbot, Publications of the Astronomical Society of Australia **36**, e010 (2019).
- [73] “The gravitational wave open science center catalog,” https://www.gw-openscience.org/eventapi/html/all_events/.
- [74] A. Bohé, L. Shao, A. Taracchini, A. Buonanno, S. Babak, I. W. Harry, I. Hinder, S. Ossokine, M. Pürrer, V. Raymond, and et al., Phys. Rev. D **95** (2017), 10.1103/physrevd.95.044028.
- [75] S. Husa, S. Khan, M. Hannam, M. Pürrer, F. Ohme, X. J. Forteza, and A. Bohé, Phys. Rev. D **93**, 044006 (2016).
- [76] S. Khan, S. Husa, M. Hannam, F. Ohme, M. Pürrer, X. J. Forteza, and A. Bohé, Phys. Rev. D **93**, 044007 (2016).
- [77] C. L. Rodriguez, B. Farr, V. Raymond, W. M. Farr, T. B. Littenberg, D. Fazi, and V. Kalogera, The Astrophysical Journal **784**, 119 (2014).
- [78] “Parameter estimation sample release for gwtc-1,” <https://dcc.ligo.org/LIGO-P1800370/public>.
- [79] S. Wu, Z. Cao, and Z.-H. Zhu, Monthly Notices of the Royal Astronomical Society **495**, 466 (2020), arXiv:2002.05528.
- [80] C. Cutler and E. E. Flanagan, Phys. Rev. D **49**, 2658–2697 (1994).
- [81] J. Lange, R. O’Shaughnessy, and M. Rizzo, “Rapid and accurate parameter inference for coalescing, precessing compact binaries,” (2018), arXiv:1805.10457 [gr-qc].
- [82] B. Abbott, R. Abbott, T. Abbott, M. Abernathy, F. Acernese, K. Ackley, C. Adams, T. Adams, P. Addesso, R. Adhikari, and et al., Phys. Rev. X **6** (2016), 10.1103/physrevx.6.041015.
- [83] J. M. Dickey, The Annals of Mathematical Statistics **42**, 204 (1971).
- [84] “Supplementary figure for monthly notices of the royal astronomical society, volume 490, issue 4, december 2019, pages 5210–5216,” https://github.com/IsobelMarguarethe/eccentric-GWTC-1/blob/master/events/GW151226/corner_all_corner.pdf ().
- [85] “Supplementary figure for monthly notices of the royal astronomical society, volume 490, issue 4, december 2019, pages 5210–5216,” https://github.com/IsobelMarguarethe/eccentric-GWTC-1/blob/master/events/GW170608/corner_all_corner.pdf ().
- [86] “TEOBResumE: Effective-one-body model with spin and tidal interactions on eccentric orbits,” https://bitbucket.org/eob_ihes/teobresums/src/eccentric/ (2021).
- [87] I. Hinder, B. Vaishnav, F. Herrmann, D. M. Shoemaker, and P. Laguna, Phys. Rev. D **77** (2008), 10.1103/physrevd.77.081502.